

Differentiable High-Performance Ray Tracing-Based Simulation of Radio Propagation with Point Clouds

Niklas Vaara, Pekka Sangi, Miguel Bordallo López, *Member, IEEE*, and Janne Heikkilä, *Senior Member, IEEE*

Abstract—Ray tracing is a widely used deterministic method for radio propagation simulations, capable of producing physically accurate multipath components. The accuracy depends on the quality of the environment model and its electromagnetic properties. Recent advances in computer vision and machine learning have made it possible to reconstruct detailed environment models augmented with semantic segmentation labels.

In this letter, we propose a differentiable ray tracing-based radio propagation simulator that operates directly on point clouds. We showcase the efficiency of our method by simulating multi-bounce propagation paths with up to five interactions with specular reflections and diffuse scattering in two indoor scenarios, each completing in less than 90 ms. Lastly, we demonstrate how the differentiability of electromagnetic computations can be combined with segmentation labels to learn the electromagnetic properties of the environment.

Index Terms—Ray tracing, differentiable simulation, radio propagation, point clouds

I. INTRODUCTION

Radio propagation simulations are an important part of research, optimization, and design of modern wireless communications systems. In the deterministic simulations, physical characteristics of the environment are used to predict radio wave propagation. One approach to such simulation is to use ray tracing (RT), which is based on determining propagation paths and their electromagnetic (EM) properties. Advances in GPU computation related to RT have made this approach increasingly efficient, and there are even applications requiring real-time RT performance. One such example is presented in [1], where a robot equipped with a software-defined radio transmits odometry updates dozens of times per second and each movement of the robot requires recomputation of propagation paths.

The accuracy of the environment model significantly influences the correctness of the simulated paths in RT. Considering geometry, traditional methods have often used hand-crafted triangle mesh models, whereas envisioned radio digital twins will utilize multi-modal sensor data to reconstruct 3D replicas of the environment [2]. Typically, sensor-based reconstructions are initially in the form of point clouds, which can be mapped to triangle meshes. Both reconstructed point clouds [3]–[7] and reconstructed triangle meshes [8]–[13] have demonstrated applicability as a basis for RT simulations. However, considering the noisiness of point clouds and computational cost of

triangle mesh mapping, it becomes more attractive to directly use point clouds in RT.

The second aspect in environment modeling is the assignment of EM material properties. Material databases available in the literature are relatively limited, one notable example being ITU-R-P.2040 [14], which contains a handful of different material parameters for multiple frequencies. Instead of using such predefined materials, recent advancements in machine learning have shown that differentiable RT, as well as neural representations combined with RT [15], [16] can be used to learn the EM material properties. Combined with point clouds, one could use semantic point cloud segmentation models such as [17], [18] to automatically label points based on their material and learn their properties using differentiable RT. Moreover, using point clusters to represent a single material may be beneficial over neural representations when the number of channel measurements is small.

RT algorithms are generally categorized into two types: the image method and ray launching [19]. The former computes exact paths for each transmitter-receiver (TX-RX) pair separately, while the latter computes approximate paths simultaneously for all TX-RX pairs by uniformly casting rays from a TX and tracing them. Environment-driven ray launching improves path computation efficiency by discretizing the environment with a given resolution and casting rays only towards these elements [5], [20]. Visibilities between all of the elements and antennas are saved in a matrix, which is expensive to compute, and thus, unsuitable for real-time applications. Moreover, the proposed methods use volumetric rays, which typically increases the number of rays to be cast after each intersection.

In this letter, our main contributions are the following: 1) An efficient ray tracer for computing paths consisting of specular reflections, diffuse scattering, and diffractions. To the best of our knowledge, our method is the first ray tracing-based method for simulating propagation paths directly on point clouds that is capable of computing multi-bounce paths in time, which is suitable for many real-time applications. Moreover, it interfaces with Sionna [21], which enables differentiable electromagnetic computations. As our method can utilize reconstructed point clouds directly, it enables the utilization of fully automated environment model construction from multi-modal sensor data. 2) An improved method for computing intersections with point clouds using surface-aligned 2D disks. Our proposed method computes a weighted average over the intersecting disks, where each weight is defined by a Gaussian on the disk plane combined with distance-based attenuation. 3) Visibility matrix-aided path computation, which enables efficient simulation of diffuse scattering, maintains a constant number of rays throughout the simulation, and

This research was supported by the Research Council of Finland (former Academy of Finland) 6G Flagship Programme (Grant Number: 346208), and the Horizon Europe CONVERGE project (Grant 101094831).

The authors are with the Center for Machine Vision and Signal Analysis, Faculty of Information Technology and Electrical Engineering, University of Oulu, Oulu, Finland.

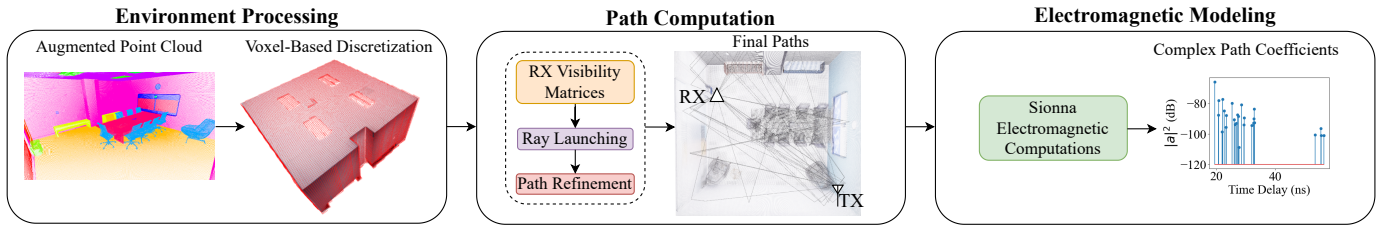


Fig. 1: Overview of how the simulator transforms the input point cloud into a ray traceable representation, followed by path and electromagnetic computations.

minimizes the effects of ray divergence. Our code is available at <https://github.com/nvaara/NimbusRT>.

II. METHOD

Our method takes an augmented point cloud as an input, where each point is associated with a 3D position \mathbf{p}_i , surface normal \mathbf{n} , surface label l_s , material label l_m . In addition, edges can be included for diffraction, described by the edge segment starting point \mathbf{e}_s ending point, \mathbf{e}_p , surface normals $[\mathbf{n}_1, \mathbf{n}_2]$, and material labels $[l_{e1}, l_{e2}]$ of the adjacent planes and that define the edge. Given a set of TX and RX positions, our method computes paths consisting of specular reflections, diffuse scattering, and diffractions, which can then be passed to Sionna for electromagnetic computations. Our method is generalizable and also supports triangle meshes, however, we focus on point clouds in this letter. An high level illustration of the method is provided in Fig. 1.

A. Pre-Processing

GPU accelerated ray tracing APIs such as OptiX [22] utilize acceleration structures for ray traversal. In the case of point clouds, we have to define a set of axis aligned bounding boxes (AABBs) and write our own implementation to determine the intersection point. Similar to our previous work [7], we discretize the point cloud into voxels with a given resolution ρ and form AABBs for each point set occupying a voxel. Each discretized point set (DPS) also contains a ray reception point, which is the mean position of all the points in the set.

B. Path Computation

Our path computation begins with visibility matrix construction. Unlike prior work [5], [20], [23], we compute visibility only from each RX to DPS ray reception points, enabling visibility matrix generation in a matter of milliseconds.

The paths are computed for each TX separately. We first cast rays to all RXs to establish the line of sight (LOS) paths. This is followed by casting rays towards all DPSs to determine the initial interaction points with the scene. Diverging from earlier works that utilize environmental information in the ray launching [5], [7], [20], the traced number of rays does not increase. Instead, each interaction is treated as a specular reflection. This allows efficient multi-bounce simulations, with near linear time complexity with respect to the number of bounces. However, the drawback is that the rays are distributed sparsely. In traditional RL this would be problematic, as the

rays would need to intersect with a volume around a RX for a path candidate to be found. In our implementation we can mitigate this problem by querying the visibility matrix to determine the path candidates for further processing.

1) *Diffusely Scattered Paths*: Diffuse scattering can be very expensive to compute as the scattered field spreads across the hemisphere. To ensure fast simulations, we support diffuse scattering as the last interaction point. As the N previous interaction points are always specular reflections, the only computation required is the final visibility validation by tracing a ray from the scatter point to the RX. Solely relying on the visibility matrix is not enough, as each DPS in the scene represents a volume rather than a surface.

2) *Specular Reflection Paths*: We compute the exact paths similarly to our previous work [7], which utilizes a path minimization approach derived from the Fermat's principle of least time. However, the refinement can be rather time consuming due to iterative ray tracing operations. To reduce this overhead, we propose a two-stage refinement process.

In the first phase, the length of a path is minimized by optimizing the interaction points on infinite boundless planes as in [23]. Mathematically, the path length can be written as

$$f_d = \sum_{k=0}^{N+1} \|\mathbf{I}_k - \mathbf{I}_{k+1}\|, \quad (1)$$

where \mathbf{I}_k is the k th point along the path trajectory. The points \mathbf{I}_0 and \mathbf{I}_{N+1} are TX and RX, respectively. We perform optimization iteratively for a maximum of ξ iterations or until convergence. A path is considered to be converged when $\|\nabla f_d\|^2 < t_c$, where the gradients represent directional derivatives along the plane vectors, which together with the normal vector of the intersection point form an orthonormal basis. In the second phase, each interaction is validated. For the k th interaction, this is done by casting a ray from \mathbf{I}_{k-1} to the optimized position. If the angular difference between the previous and new surface normal and the distance to the previous intersection point plane defined by its surface normal are below the thresholds t_a and t_d , the path is considered valid. Otherwise, we retry the optimization κ times.

3) *Diffacted Paths*: Diffacted paths are computationally expensive, as the wave that encounters an edge scatters in multiple directions following the shape of a Keller's cone [24]. Similarly to diffuse scattering, one could utilize the visibility matrix to validate the visibility from an edge to RXs. However, since Sionna is restricted to single-bounce diffractions, our implementation follows this restriction. As a result, for each

edge, we simply minimize the path length similar to specular reflections, as explained in Section II-B2. Lastly, we validate that the edge is visible from both TX and RX.

4) *Duplicate Path Removal*: As many of the paths converge to the same trajectory, a lot of duplicate paths will be present. We follow the hashing implementation of [7] where the path interaction type and the surface labels l_s of the closest points at each intersection are used to form a unique hash per path trajectory. In the case of diffuse scattering we instead use the voxel coordinate for hashing, as each surface may have multiple valid scatter points. Thus, each diffusely scattered path represents the scattered field over an area of size ρ^2 , approximating the area of the voxel resolution ρ .

C. Intersection Computation

In our previous work [7], we utilized a signed distance function (SDF) to model the implicit surface of a DPS. Finding the zero-level set of the SDF requires iterative ray marching, which may take many iterations to converge. Each point contribution was calculated using the spherically attenuating Gaussian weight function

$$\delta(\mathbf{s}) = \exp\left(-\frac{\|\mathbf{p}_i - \mathbf{s}\|^2}{2\sigma^2}\right), \quad (2)$$

where \mathbf{s} is the sample position at which the SDF is evaluated and σ is the attenuation factor. This function does not align well with the actual surface geometry, and the points are not explicitly intersectable.

To account for these limitations, we propose an alternative approach for computing ray-surface intersections. Each point in a DPS is represented as a planar disk, whose centroid is \mathbf{p}_i , normal is $\hat{\mathbf{n}}_i$, and radius is given by a parameter r_p . This enables the evaluation of explicit ray-disk intersection \mathbf{q}_i for each point in the DPS for a given ray. Finally, the surface intersection point is computed as the weighted average of the intersected disks in the DPS with

$$\mathbf{q} = \frac{\sum_i \mathbf{q}_i \omega_i}{\sum_i \omega_i}, \quad (3)$$

where ω_i denotes the weight of the i th intersected disk. The weights are computed using

$$\omega_i = \exp\left(-\frac{\|\mathbf{q}_i - \mathbf{p}_i\|^2}{2r_p^2}\right) \exp(-\lambda_d \|\mathbf{q}_i - \mathbf{q}_{min}\|), \quad (4)$$

where \mathbf{q}_{min} is the ray-disk intersection point closest to the ray origin, and $\lambda_d > 0$ is a depth attenuation parameter. The parameter λ_d can be used to adapt to the noisiness of the point cloud, while r_p can be based on the point cloud density.

III. EXPERIMENTS

In these experiments we demonstrate the efficiency of our simulator and how it can be used to leverage the differentiable EM computations of Sionna. The experiments were conducted on a computer equipped with an NVIDIA GeForce RTX 3080 GPU, and with the parameters presented in Table I.

TABLE I: Generic simulation parameters.

Name	Parameter	Value
Voxel Size	ρ	0.0625
Point Radius	r_p	0.015
Distance Attenuation	λ_d	100
Refine Max Iterations	ξ	50
Refine Retry Iterations	κ	10
Refine Convergence Threshold	t_c	0.0001
Refine Angle Threshold	t_a	1.0
Refine Distance Threshold	t_d	0.01

A. Performance Evaluation

We evaluate our method against [7] and use the same corridor scene (see Fig. 2a) by benchmarking the simulation with 2–5 specular reflections in non-LOS conditions. We use the results achieved with voxel size of 0.5 m from [7] as the baseline, since the smallest discretization size matches our voxel size. From the results shown in Table II it can be observed that the baseline method [7] starts to slow down rapidly after the number of interactions is increased, while our simulator is capable of finding similar amount of specular paths while maintaining fast execution time. In addition, including diffuse scattering causes only a small computational overhead.

It should be noted that in [7] refinement was computed with 2000 iterations without any convergence-based exit condition and therefore, to have a clearer comparison, the coarse path computation and refinement are separated in Table II. Our method computes the refined paths after every bounce, while in [7] it is done for all of the coarse paths at once. The implementation of [7] is suited for more complex simulations such as paths consisting of multiple diffractions, while the main focus of the method presented here is rapid simulations. However, it can also simulate single bounce diffractions with negligible overhead.

For further evaluation, we performed a simulation with maximum interaction depth of 5 in the Replica *room 0* shown in Fig. 2b, with the illustrated TX position and six RX positions. With specular reflections and diffuse scattering enabled, our method achieved a path computation time of 81–88 ms per link, with an average computation time of 85 ms.

B. Learning Electromagnetic Properties from Material Labels

In this experiment, we showcase how the relative permittivities, conductivities, and scattering coefficients of the material labels could be learned. For the environment model, the *room 0* scene from Replica [25] was chosen. The dataset contains rich geometric information such as class and instance segmentation labels. We use the former labels for the material labels l_m , while the latter are used as surface labels l_s . For visualization purposes, we reduce the total number of materials to five. The paths are simulated up to two interactions, including diffuse scattering with Lambertian scattering model [26], specular reflections, and LOS at six different RX locations (see Fig. 2b). This results in an average of just over 44 000 paths per link.

As the ground truth for training, channel impulse responses (CIRs) are synthetically generated by computing channel frequency responses (CFRs) using 129 equally spaced samples over a 1.5 GHz bandwidth centered at 8 GHz. The complex



(a) The corridor scene and baseline method from [7] are used for performance evaluation.

(b) An indoor scene from Replica dataset [25], which is used for demonstrating the learning of material properties based on material labels.

Fig. 2: Scenes and antenna positions used in the experiments.

path coefficients are computed at this center frequency. The CIRs and CFRs can be obtained from the path coefficients as shown e.g. in [4].

During each train iteration, one of the RX positions shown in Fig. 2b is chosen randomly and we compute the CIR from the simulated paths. We use Adam optimizer with a learning rate of 0.01 and optimize the material parameters with the loss

$$\mathcal{L} = \frac{|\mathbf{h} - \hat{\mathbf{h}}|^2}{|\hat{\mathbf{h}}|^2}, \quad (5)$$

where \mathbf{h} and $\hat{\mathbf{h}}$ are the simulated and ground truth CIR, respectively. Additionally, we apply appropriate activation functions to the optimizable parameters in order to constrain them within their valid ranges. We perform the optimization for 5000 iterations. The results are illustrated in Fig. 3, which showcases the parameters at each training iteration, and that the parameters can be recovered accurately. The rightmost

figure illustrates the ground truth power delay profile (PDP) and the respective one with learned parameters.

IV. CONCLUSION

In this letter we presented a ray tracing-based method for simulating radio propagation with point clouds. We demonstrated the efficiency of our method, which was capable of computing multi-bounce paths in less than 90 ms in the experimental cases, having close to linear growth in terms of computational complexity as the interaction depth was increased. We also showcased how the differentiability of electromagnetic computations could be leveraged together with segmentation labels to learn material parameters from ground truth channel impulse responses.

Future work will focus on further experiments with segmented point clouds constructed from multi-modal sensor data and utilizing real world channel measurements for material parameter estimation.

TABLE II: Performance evaluation of our method with specular reflections and diffuse scattering in the corridor scene.

Max. Depth	Vaara <i>et al.</i> [7], Specular Paths			Ours, Specular Paths		Ours, Specular + Scattered Paths	
	Trace (ms)	Refine (ms)	Num. Paths	Trace + Refine (ms)	Num. Paths	Trace + Refine (ms)	Num. Paths
2	30	330	9	10	9	18	17 393
3	60	600	25	15	25	25	26 681
4	510	1100	52	21	53	37	36 637
5	7650	2800	90	28	89	52	47 403

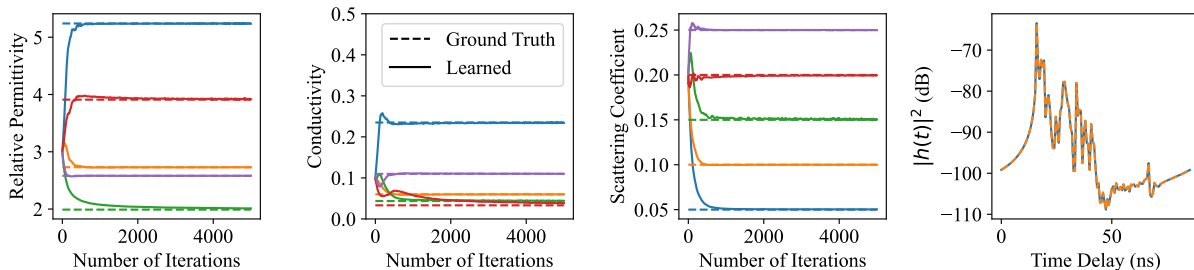


Fig. 3: Relative permittivity, conductivity, and scattering coefficient at each training iteration. The rightmost figure shows the ground truth PDP and the PDP computed with the trained materials after 5000 iterations between TX and RX2 in the Replica room 0 scene (see Fig. 2b).

REFERENCES

- [1] V. C. Andrei, P. Susarla, A. Djuhera, N. Vaara, J. Mustaniemi, C. Á. Casado, X. Li, U. J. Mönich, H. Boche, and M. Bordallo López, “Demonstration of a continuously updated, radio-compatible digital twin for robotic integrated sensing and communications,” in *2025 IEEE 5th International Symposium on Joint Communications & Sensing (JC&S)*. IEEE, 2025, pp. 1–2.
- [2] A. Alkhateeb, S. Jiang, and G. Charan, “Real-time digital twins: Vision and research directions for 6g and beyond,” *IEEE Communications Magazine*, 2023.
- [3] U. T. Virk, J.-F. Wagen, and K. Haneda, “Simulating specular reflections for point cloud geometrical database of the environment,” in *2015 Loughborough Antennas & Propagation Conference (LAPC)*. IEEE, 2015, pp. 1–5.
- [4] J. Järveläinen, K. Haneda, and A. Karttunen, “Indoor propagation channel simulations at 60 GHz using point cloud data,” *IEEE Transactions on Antennas and Propagation*, vol. 64, no. 10, pp. 4457–4467, 2016.
- [5] P. Koivumäki and K. Haneda, “Point cloud ray-launching simulations of indoor multipath channels at 60 GHz,” in *2022 IEEE 33rd Annual International Symposium on Personal, Indoor and Mobile Radio Communications (PIMRC)*. IEEE, 2022, pp. 01–07.
- [6] P. Koivumäki, A. Karttunen, and K. Haneda, “Ray-optics simulations of outdoor-to-indoor multipath channels at 4 and 14 ghz,” *IEEE Transactions on Antennas and Propagation*, 2023.
- [7] N. Vaara, P. Sangi, M. Bordallo López, and J. Heikkilä, “Ray launching-based computation of exact paths with noisy dense point clouds,” *IEEE Transactions on Antennas and Propagation*, 2025.
- [8] M. Pang, H. Wang, K. Lin, and H. Lin, “A gpu-based radio wave propagation prediction with progressive processing on point cloud,” *IEEE Antennas and Wireless Propagation Letters*, vol. 20, no. 6, pp. 1078–1082, 2021.
- [9] T. Wahl, D. Borrmann, M. Bleier, A. Nüchter, T. Wiemann, T. Hänel, and N. Aschenbruck, “Wip: Real-world 3d models derived from mobile mapping for ray launching based propagation loss modeling,” in *2022 IEEE 23rd International Symposium on a World of Wireless, Mobile and Multimedia Networks (WoWMoM)*. IEEE, 2022, pp. 161–164.
- [10] N. Suga, Y. Maeda, and K. Sato, “Indoor radio map construction via ray tracing with RGB-D sensor-based 3D reconstruction: Concept and experiments in WLAN systems,” *IEEE Access*, vol. 11, pp. 24 863–24 874, 2023.
- [11] A. Kamari, N. Wu, H. K. Narsani, B. Han, and P. Pathak, “Environment-driven mmwave beamforming for multi-user immersive applications,” in *Proceedings of the 1st ACM Workshop on Mobile Immersive Computing, Networking, and Systems*, 2023, pp. 268–275.
- [12] G. Xia, C. Zhou, F. Zhang, Z. Cui, C. Liu, H. Ji, X. Zhang, Z. Zhao, and Y. Xiao, “Path loss prediction in urban environments with sionnart based on accurate propagation scene models at 2.8 ghz,” *IEEE Transactions on Antennas and Propagation*, 2024.
- [13] N. Suga, N. Yoshida, R. Gozono, Y. Maeda, and K. Sato, “Rbg-d sensor-aided radio map estimation using materials classification,” *IEEE Wireless Communications Letters*, 2025.
- [14] “ITU-R P.2040,” <https://www.itu.int/rec/R-REC-P.2040/en>, accessed: 24.04.2025.
- [15] J. Hoydis, F. A. Aoudia, S. Cammerer, F. Euchner, M. Nimier-David, S. Ten Brink, and A. Keller, “Learning radio environments by differentiable ray tracing,” *IEEE Transactions on Machine Learning in Communications and Networking*, 2024.
- [16] S. Jiang, Q. Qu, X. Pan, A. Agrawal, R. Newcombe, and A. Alkhateeb, “Learnable wireless digital twins: Reconstructing electromagnetic field with neural representations,” *IEEE Open Journal of the Communications Society*, 2025.
- [17] J. Schult, F. Engelmann, A. Hermans, O. Litany, S. Tang, and B. Leibe, “Mask3d: Mask transformer for 3d semantic segmentation,” in *2023 IEEE International Conference on Robotics and Automation (ICRA)*. IEEE, 2023, pp. 8216–8223.
- [18] M. Kolodiaznyi, A. Vorontsova, A. Konushin, and D. Rukhovich, “Oneformer3d: One transformer for unified point cloud segmentation,” in *Proceedings of the IEEE/CVF Conference on Computer Vision and Pattern Recognition*, 2024, pp. 20 943–20 953.
- [19] Z. Yun and M. F. Iskander, “Ray tracing for radio propagation modeling: Principles and applications,” *IEEE Access*, vol. 3, pp. 1089–1100, 2015.
- [20] J. S. Lu, E. M. Vitucci, V. Degli-Esposti, F. Fuschini, M. Barbiroli, J. A. Blaha, and H. L. Bertoni, “A discrete environment-driven GPU-based ray launching algorithm,” *IEEE Transactions on Antennas and Propagation*, vol. 67, no. 2, pp. 1180–1192, 2018.
- [21] J. Hoydis, F. A. Aoudia, S. Cammerer, M. Nimier-David, N. Binder, G. Marcus, and A. Keller, “Sionna RT: Differentiable ray tracing for radio propagation modeling,” *arXiv preprint arXiv:2303.11103*, 2023.
- [22] S. G. Parker, J. Bigler, A. Dietrich, H. Friedrich, J. Hoberock, D. Luebke, D. McAllister, M. McGuire, K. Morley, A. Robison *et al.*, “OptiX: A general purpose ray tracing engine,” *ACM Transactions on Graphics*, vol. 29, no. 4, pp. 1–13, 2010.
- [23] N. Vaara, P. Sangi, J. Pyhtilä, M. Juntti, and J. Heikkilä, “A refined path generation pipeline for radio channel propagation modeling,” in *2023 17th European Conference on Antennas and Propagation (EuCAP)*. IEEE, 2023, pp. 1–5.
- [24] J. B. Keller, “Geometrical theory of diffraction,” *Josa*, vol. 52, no. 2, pp. 116–130, 1962.
- [25] J. Straub, T. Whelan, L. Ma, Y. Chen, E. Wijmans, S. Green, J. J. Engel, R. Mur-Artal, C. Ren, S. Verma *et al.*, “The replica dataset: A digital replica of indoor spaces,” *arXiv preprint arXiv:1906.05797*, 2019.
- [26] V. Degli-Esposti, F. Fuschini, E. M. Vitucci, and G. Falciaisecca, “Measurement and modelling of scattering from buildings,” *IEEE transactions on antennas and propagation*, vol. 55, no. 1, pp. 143–153, 2007.